metals

Article

Microstructural Evolution in the Stir Zone of a Friction-Stir-Processed Microalloyed Al-Mn-Cu Alloy

Franc Zupanič [1], Pamela Marcela Pineda Dominguez [2], Yan Lu [3], Torben Boll [2], Rafal Dunin-Borkowski [3], Lara Hočuršćak [1], Evelin Fisslthaler [4], Damjan Klobčar [5] and Tonica Bončina [1,*]

[1] Faculty of Mechanical Engineering, University of Maribor, 2000 Maribor, Slovenia; franc.zupanic@um.si (F.Z.)
[2] Karlsruhe Nano Micro Facility (KNMFi), Karlsruhe Institute of Technology, 76344 Eggenstein-Leopoldshafen, Germany
[3] Ernst Ruska-Centre for Microscopy and Spectroscopy with Electrons, Forschungszentrum Jülich GmbH, 52425 Jülich, Germany; y.lu@fz-juelich.de (Y.L.); rdb@fz-juelich.de (R.D.-B.)
[4] Graz Centre for Electron Microscopy, 8010 Graz, Austria; evelin.fisslthaler@felmi-zfe.at
[5] Faculty of Mechanical Engineering, University of Ljubljana, 1000 Ljubljana, Slovenia; damjan.klobcar@fs.uni-lj.si
* Correspondence: tonica.boncina@um.si

Abstract

The study investigates the microstructure evolution in the stir zone produced by the friction stir processing (FSP) of a heat-treated microalloyed Al-Mn-Cu alloy in the area subjected to the highest temperature, strain, and strain rate. The samples were studied using electron microscopy and atom probe tomography (APT) to obtain structural and chemical information from the macro to the nano scale. FSP refines the dendritic Al-rich solid solution grains through dynamic recrystallisation in the range of a few micrometres. The primary intermetallic phases were dispersed to the particles in the 0.5–3 μm range and transformed mainly into a more stable τ_1-$Al_{29}Mn_6Cu_4$ phase. The fraction of dispersed particles after FSP increased due to the precipitation from the solid solution during cooling. The nanoscale quasicrystalline precipitates in the matrix, formed upon heat treatment, dissolved entirely during FSP, while the strong coarsening of the $L1_2$ precipitates occurred due to high temperatures in the stir zone. After FSP, the hardness of the stir zone was nearly identical for specimens in the as-cast and heat-treated conditions.

Keywords: microscopy; friction stir processing; aluminium; microstructure; atom probe tomography

Academic Editor: Noé Cheung

Received: 27 February 2026
Revised: 19 March 2026
Accepted: 21 March 2026
Published: 23 March 2026

1. Introduction

Friction stir processing (FSP) and welding (FSW) of aluminium alloys are prevalent in the automotive and aerospace industries, because they offer many advantages over fusion welding. Friction stir processing (FSP) is a thermomechanical process in which the material is exposed to extreme plastic deformation and a high temperature due to the transformation of mechanical work to heat [1]. A rotating, non-consumable tool with a pin is inserted into the workpiece and moves over the material's surface [2]. The FSP-treated material consists of the stir zone (SZ), thermomechanically affected zone (TMAZ), and heat-affected zone (HAZ). Different microstructures can form in each zone, due to the differences in the degree of plastic deformation, deformation rate, and thermal history [3].

The highest temperatures, strains, and strain rates were observed in the SZ, which is the focus of this investigation. They cause extraordinary grain refinement via dynamic

recovery and recrystallisation [4], the dissolution of precipitates [5], the dissolution and fragmentation of thermally stable phases [6], and the removal of the casting and other defects [7]. In AA2024-T351 aluminium alloy, the S-phase (Al_2CuMg) and Guinier–Preston–Bagaryatsky (GPB) zones are prone to dissolution during the thermal cycles induced by welding. However, the GPB zones and metastable S-phase needles reprecipitated in the SZ contribute to the hardness recovery [8]. In the AA2219-T8 alloy, the precipitates also dissolve in the HAZ and TMAZ, even though the temperatures are much lower in the SZ, but do not reprecipitate during cooling due to elevated temperatures [9]. Reprecipitation can also occur during the post-weld heat treatment. In the 2195-O Al–Li alloy, solution treatment followed by artificial ageing enables the complete dissolution of coarse precipitates and the precipitation of strengthening phases (T1-Al_2CuLi and θ'-Al_2Cu) in the SZ [10].

The fragmentation and even dissolution of thermally stable phases can occur in the SZ. High strain gradients and pipe diffusion along the dislocations can increase the diffusivity of Y in the Mg matrix by 60 times. The dissolution can be enhanced by the mechanism of dislocation sweeping, which involves (i) the thermally activated diffusion of a solute atom into the dislocation core, (ii) the transportation of the solute atom along the core by pipe diffusion, and (iii) the detachment of the dislocation from the particle with the solute at a rate equal to the dislocation velocity. The fragmentation of a particle occurs when the stress required for nucleating dislocations within the particle exceeds the particle's fracture stress. Otherwise, the particle dissolves [6].

Fragmentation and dispersion take place for both the in situ formed phases (e.g., during solidification) and the ex situ added particles (e.g., to produce gradient structures [11,12]). Brittle particles with incoherent interfaces, especially when agglomerated, serve as crack initiation sites, degrading the mechanical properties significantly. In 7A52 aluminium alloy, the incoherent Mg_2Si phase and AlFe phase act as crack initiation sites and crack propagation paths in the TMAZ, while the semi-coherent AlMgCu phase hinders the movement of dislocations and improves the mechanical properties of the joints [13]. The coarse and incoherent secondary phases (size around 10 μm) are the preferred crack initiation sites, and the crack tends to propagate along the path where the coarse secondary phases are dense [14]. The processing parameters in FSP/FSW, such as the rotational speed, travel speed, and heat input, play a critical role in determining the extent of the phase transformation, since the strain, strain rate, and temperature distribution depend on these parameters [15,16].

There is little information on the quasicrystalline phases in alloys treated by FSP and FSW. Macerl et al. [17] reported on the transformation of the metastable eutectic IQC phase to a stable τ_1-$Al_{29}Mn_6Cu_4$ phase in an $Al_{94}Mn_2Cu_2Be_2$ alloy. The IQC phase (Mg_3Zn_6Y) was also present in a magnesium Mg-Zn-Y-Zr alloy [18]. During FSP, the IQC phase transformed into the face-centred cubic W phase ($Mg_3Zn_3Y_2$). The larger IQC particles were dispersed and enveloped by the W-phase shell, indicating an only partial transformation.

In the last few decades, considerable attention has been paid to the development of Al alloys containing $L1_2$ precipitates, due to their beneficial effects on mechanical and other properties [19–21]. Some research work stated the high resistance of $L1_2$ precipitates during FSP or FSW. In the Al–Mg–Sc alloy, the Al_3Sc precipitate size and density remained almost unchanged in the SZ compared to the base alloy [22]. These precipitates reduced the boundary mobility of the recrystallised grains strongly, leading to a very small grain size. The high stability of the $L1_2$ precipitates led to superplastic behaviour in an Al-3Mg-0.1Sc-0.1Zr alloy [23] and in Al-Mg-Si-Zr-Sc alloys [24].

Recently, novel experimental alloys based on the Al-Mn-Cu system were developed containing quasicrystalline and $L1_2$ precipitates [25]. Both quasicrystalline and $L1_2$ are much more thermally stable than the typical strengthening phases in the

precipitation-hardened aluminium alloys. Their combination was obtained by T5 heat treatment. This direct artificial ageing follows casting, and provides a sufficient cooling rate to preserve the supersaturation of the alloying elements in the aluminium-rich matrix. In this work, we investigated a microalloyed Al-Mn-Cu alloy. It contained Mn to form quasicrystalline precipitates [26], and Be to increase their number density enormously [9]. Sc and Zr were added to form $L1_2$ precipitates [25], while Cr and V are supposed to improve the thermal stability. Understanding the microstructural evolution and redistribution of alloying elements during FSP in the SZ of this multicomponent, multiphase alloy is of the utmost importance for its further development. To date, there are no reports dedicated to the behaviour of quasicrystalline precipitates in aluminium alloys during friction stir processing/welding.

According to the above overview, the main hypothesis assumes that the quasicrystalline and $L1_2$ precipitates will remain stable during FSP. Thus, they will prevent (i) the softening of the SZ, (ii) as well as the softening in the HAZ, which, typically, happens in many precipitation-strengthened Al alloys. The secondary goal was to determine the Be distribution, which has not been determined yet. Scanning and transmission electron microscopy, as well as atom probe tomography, were applied to obtain reliable information over different length scales. The APT enabled us to determine the beryllium distribution in this microalloyed Al-Mn-Cu alloy for the first time.

2. Materials and Methods

The composition of the investigated Al alloy was 2.18% Mn, 2.73% Cu, 0.18% Sc, 0.08% Be, 0.16% Zr, 0.08% Cr, 0.16% Fe, 0.0003% Mg, 0.009% Ti, and 0.07% V. The values are in wt.%, and were determined using Agilent 7900 ICP-MS (Agilent Technologies, Inc., Santa Clara, CA, USA). The alloy was prepared by melting Al 99.8 and several master alloys (AlBe5.5, AlCr20, AlV10, AlZr10, AlSc2, AlCu50, and AlMn10) in an electric-resistance furnace (Bosio, Bukovžlak, Slovenia), and casting at 750 °C into a copper mould with the dimensions 100 mm × 60 mm × 6 mm. The heat treatment was carried out in the air at 330 °C for 24 h, and then at 450 °C for 30′ to obtain an appropriate distribution of the icosahedral and $L1_2$ precipitates in the Al-rich matrix.

The alloy, in both the as-cast and heat-treated conditions, was subjected to FSP using a steel tool (H13 grade) on a universal milling machine (Prvomajska ALG 200, Prvomajska, Zagreb, Croatia). The dimensions of the processed parts were 100 mm × 25 mm × 6 mm. The tool dimensions were 17 mm shoulder diameter, 4 mm pin diameter, and 3.5 mm pin length. The typical plunge depth was 0.4 mm, and the tool tilt angle was 0°. In the preliminary experiments, several combinations of traverse and rotational speeds were tested. The most reliable results were obtained with a pin traverse speed of 46 mm/min and a rotational speed of 475 min^{-1}. Three FSP trials were done with each testing condition. The temperatures were measured during the tests using thermocouples at different distances from the SZ.

The investigations were carried out from the macro to the nano scale to study the microstructure and chemical composition systematically. The specimens were ground mechanically, polished, and etched optionally with Weck's reagent. The macrographs were taken with an Olympus SZX10 microscope (Olympus, Tokyo, Japan). Scanning electron microscopy (SEM) with a backscatter electron (BSE) detector was used for the bulk samples to reveal the compositional differences. The SEM was performed in a JSM-IT800 SHL (Jeol, Tokyo, Japan) equipped with an energy-dispersive X-ray spectrometer (EDS) (Oxford Instruments, High Wycombe, UK). The BSE imaging and EDS analysis were carried out at an accelerating voltage of 10 kV. More about the metallography of the quasicrystalline phases is given elsewhere [27].

The X-ray diffraction was performed at the synchrotron Elettra (Sincrotrone Elettra, Trieste, Italy) using X-rays with a wavelength of 0.0999996 nm. The XRD images were taken in a transmission mode at 24 °C. The samples were thin plates with a thickness of about 250 µm. The 2D images were collected using a Dectris Pilatus 2M camera (Dectris Ltd., Baden, Switzerland) at a working distance of 100 mm. More details can be found in Ref. [17].

The TEM sample in the heat-treated condition before FSP was prepared by ion milling using a Gatan PIPS II (Gatan, Inc., Pleasanton, CA, USA), while the sample after FSP was taken at the specific site using an FEI NanoLab 460F1 (FEI, Eindhoven, The Netherlands). For the nanoscale study, the microstructure and chemical composition analyses were studied using high-angle angular dark field (HAADF) scanning transmission electron microscopy STEM in an FEI Titan G2 80-200 ChemiSTEM (FEI, Eindhoven, The Netherlands) and FEI Titan^3 G2 80-300 (FEI, Eindhoven, The Netherlands). The EDS mapping was carried out using a Super-X detector (Thermo Fisher Scientific, Waltham, MA, USA) at 200 and 300 keV. The APT experiments were conducted using a Cameca® Local Electrode Atom Probe (LEAP 4000X HR) (Cameca Atom Probe Technology Center, Madison, WI, USA) system equipped with a UV laser (~355 nm) to investigate the three-dimensional distribution of the light elements further. The temperature was set to 30 K, with a detection rate of 0.3%, a pulse frequency of 200 kHz, and a laser beam energy of 20 pJ. The specimens studied in the APT were prepared by electropolishing, and sharpened using a focused ion beam (FIB) system in a Zeiss® Auriga 60© (Carl Zeiss Microscopy GmbH, Jena, Germany) and a Tescan Solaris X© scanning electron microscope (Tescan Group, Brno, Czech Republic).

The grain sizes were determined from light micrographs using the linear-intercept method. The phase analysis and particle distributions were performed using three SEM or TEM images at appropriate magnifications in ImageJ 1.54 g (https://imagej.net/, accessed on 1 March 2026). The particle distribution in SZ was measured using three images at a magnification of 5000× in the Analyse Particles module of ImageJ, after applying an appropriate threshold.

The microhardness HV 0.1 was measured using a DuraScan 50 (Emco-Test Prüfmaschinen GmbH, Kellau, Kuchl, Austria) with the following parameters: load 0.981 N, indent spacing 0.5 mm, and a dwell time at the maximum load of 12 s.

3. Results

3.1. Microstructure in the As-Cast and Heat-Treated Conditions

The alloy's microstructure in the as-cast condition consisted of dendritic Al-rich grains α-Al and several phases in the interdendritic regions (Figure 1a). The sizes of the equiaxed grains were 120 ± 15 µm, and the secondary dendrite arm spacing was 12 ± 3 µm. It was determined using linear-intercept methods on five light-microscopic images taken at lower magnification. The matrix was supersaturated with approximately 0.8% Mn, 2% Cu, 0.2% Sc, and 0.1% Zr (in wt.%). The intermetallic phases in the interdendritic regions were identified as Θ-Al_2Cu, which contained about 3 at.% Sc (the brightest phase in Figure 1a), and Mn-rich particles with an approximate composition Al_4Mn also containing 2–3 at.% Cu, around 2 at.% Fe, and some Cr. Some particles were identified as icosahedral quasicrystals (IQCs), forming a typical two-phase structure, while others were quasicrystalline approximants, likely $Al_{15}Mn_3Be_2$. The fraction of Θ-Al_2Cu was 1.92 ± 0.18%, and the remaining Mn-rich phases were 2.74 ± 0.23%. Despite quite a low volume fraction of minor phases, the XRD identified Θ-Al_2Cu clearly, and some peaks may be attributed to $Al_{15}Mn_3Be_2$ and IQCs (Figure 2).

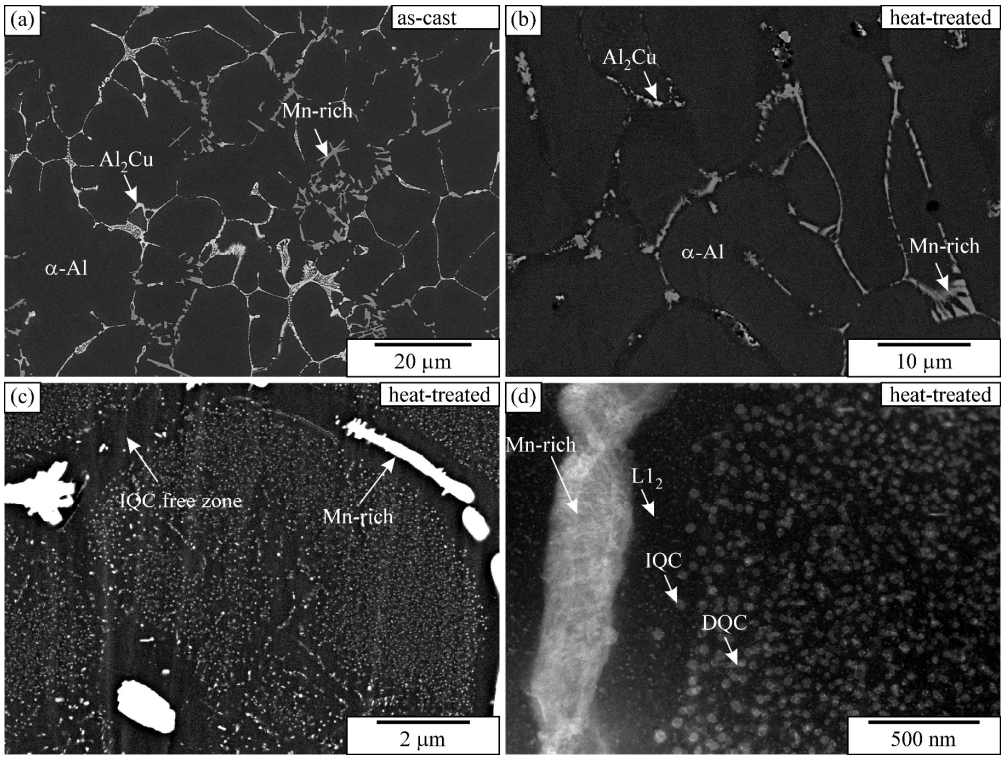

Figure 1. Microstructure of the alloy in the as-cast and heat-treated conditions: (**a**) as-cast condition (backscattered electron image—SEM BSE), (**b**,**c**) SEM micrographs of heat-treated condition at different magnifications (SEM BSE), and (**d**) TEM micrograph of heat-treated condition (STEM HAADF). BSE and HAADF images reveal a brighter contrast for elements with higher atomic numbers and a darker contrast for elements with lower atomic numbers.

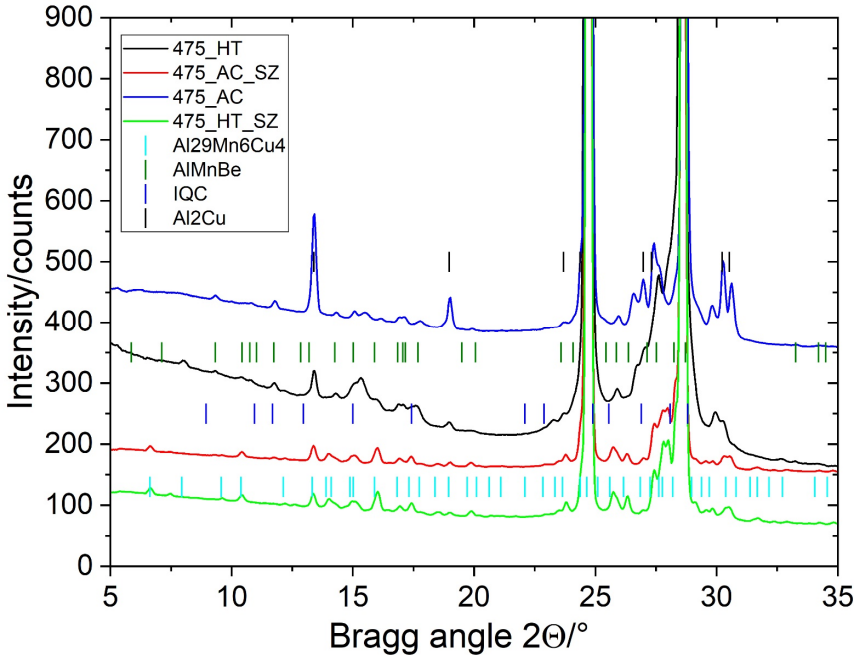

Figure 2. XRD spectra of samples in different conditions (AC—as-cast, HT—heat-treated, AC–SZ—stir zone of the as-cast sample, and HT–SZ—stir zone of the heat-treated sample).

The heat treatment did not cause any differences in the grain sizes and dendritic arm spacing. However, the fraction of Θ-Al_2Cu dropped to just 0.25 ± 0.08%, while the fraction of the Mn-rich phases remained almost the same, 2.61 ± 0.17%. The solubility of

copper increases with the temperature; thus, the Θ-Al_2Cu dissolved (Figure 1b). The XRD pattern shows a clear decrease in Θ-Al_2Cu peaks (Figure 2). Numerous precipitates formed during the heat treatment (Figure 1c,d), which were identified as icosahedral and decagonal quasicrystals, and ordered $L1_2$-Al_3(Sc, Zr) (Figure 3). The quasicrystalline precipitates were present throughout the dendrites, and there was a quasicrystalline precipitation-free zone (PFZ) in the interdendritic region. The quasicrystalline precipitates exhibited predominantly an icosahedral structure, with a spheroidal shape and a diameter of 26 ± 3 nm. They were slightly elongated along their twofold directions in the <001> directions of the α-Al. The FFT showed clearly that the twofold axis $[001\bar{1}0]$ was parallel to the fourfold [001] direction of the α-Al, and that the other twofold directions were parallel to the fourfold directions of the α-Al. The {221001} planes coincided with the {002} planes of the α-Al, indicating the same interplanar distances of the IQC and α-Al (Figure 3a–c). In such a case, the threefold axis of the α-Al [111] should also be parallel to the threefold axis of the IQC $[0\,1\,1\,0\,\bar{1}\,0]$ [25] (the indices are according to Singh and Ranganathan [28]). The same orientation relationship between the α-Al and IQC was found in a melt-spun Al-Mn-Si alloy [29]. Platelike decagonal quasicrystalline precipitates (DQCs) accounted for a smaller fraction of the precipitates (Figure 3d,e). In most cases, their habitus planes were parallel to the {001} planes of the α-Al. The DQC precipitates with this habitus plane can adopt three different orientations relative to the matrix. The precipitates on the (001) plane of the α-Al had a tenfold axis parallel to the [010] direction of the α-Al and a twofold axis parallel to the [100] direction of the α-Al.

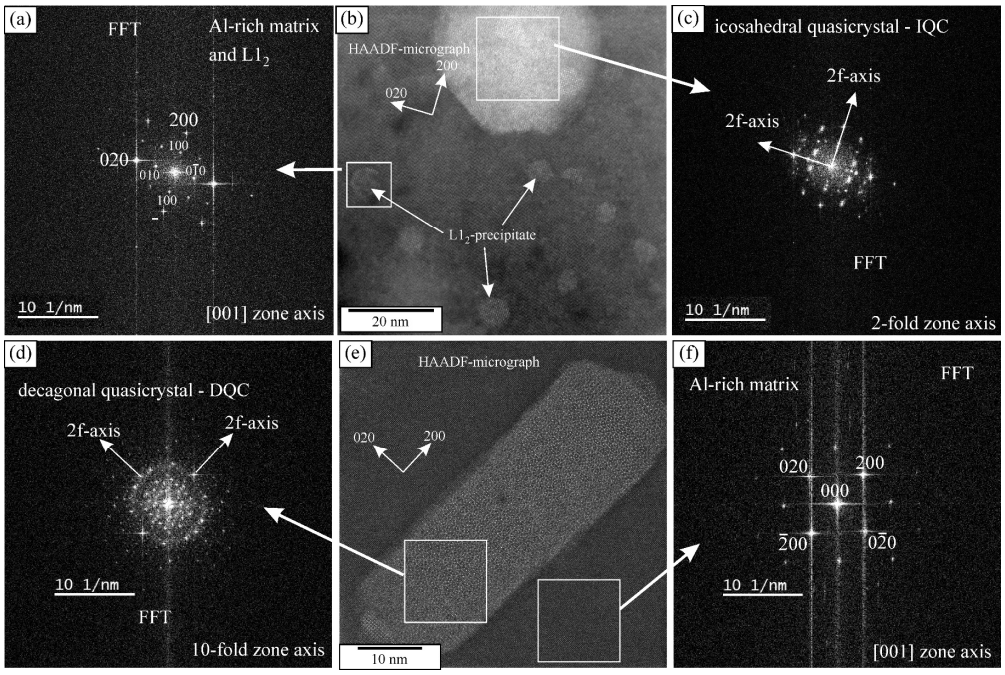

Figure 3. Icosahedral quasicrystal and $L1_2$ precipitates in the α-Al matrix after heat treatment: (**a**) the FFT of the $L1_2$ precipitate and Al-rich matrix, (**b**) HAADF micrograph, (**c**) Fast Fourier Transform (FFT) of the icosahedral quasicrystal, (**d**) Fast Fourier Transform (FFT) of the decagonal quasicrystal, (**e**) decagonal quasicrystal in the α-Al matrix after heat treatment, and (**f**) FFT of the Al-rich matrix.

The $L1_2$ precipitates were the most abundant. They were present in the spaces between the IQC and DQC precipitates and in the IQC precipitation-free zone. The core-shell precipitates had a cuboidal shape. The $L1_2$ precipitates were coherent with the α-Al, as they had a cube-on-cube orientation relationship with the α-Al matrix, as found in a previous publication [25]. The number density of $L1_2$ was 2.8×10^{22} m^3, which is much higher

than the number density of the IQC precipitates, but less than in high-strength aluminium alloys [30].

The quasicrystalline particles, both IQCs and DQCs, contained mainly Mn, with some Cu. The $L1_2$ precipitates contained Sc and Zr, while the other elements were distributed evenly in the particles and matrix (Figure 4).

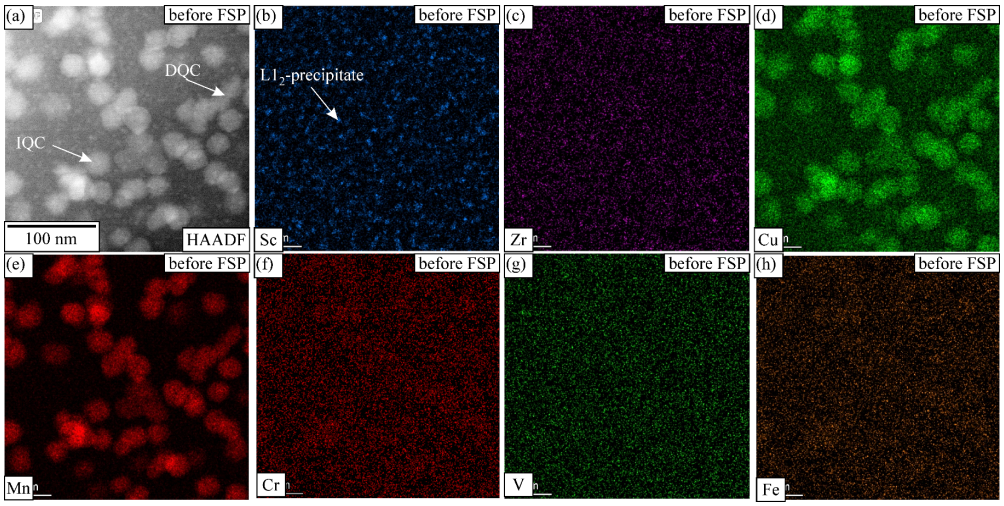

Figure 4. STEM EDS mapping of the heat-treated sample inside a crystal grain, with each element mapping displayed by intensity. The investigated area includes the phases IQC, DQC, and $L1_2$. (**a**) HAADF image, elemental maps of (**b**) Sc, (**c**) Zr, (**d**) Cu, (**e**) Mn, (**f**) Cr, (**g**) V and (**h**) Fe.

The combination of SEM EDS and STEM EDS enabled us to obtain information regarding the shape, size, and distribution of the microstructural constituents and all the elements except for Be, with the lowest atomic number. It was present in relatively small quantities, lower than the EDS detection limit. Information about Be and the distribution of all the other elements at the atomic scale was obtained by APT. Figure 5 shows a small region encompassing an IQC precipitate and an Al-rich matrix. The IQC precipitate contains Mn and Cu, as found previously, but also Be. There was also a tiny amount of Be in the Al-rich matrix. Figure 5 also shows the $L1_2$-Al_3X precipitates containing Sc and Zr. The distribution of Sc and Zr in the proxigrams shows the enrichment of Zr around Sc, indicating the adjacent segregation of Zr in the shell and a slight tendency to form a core-shell structure in $L1_2$-Al_3X, as found by [31].

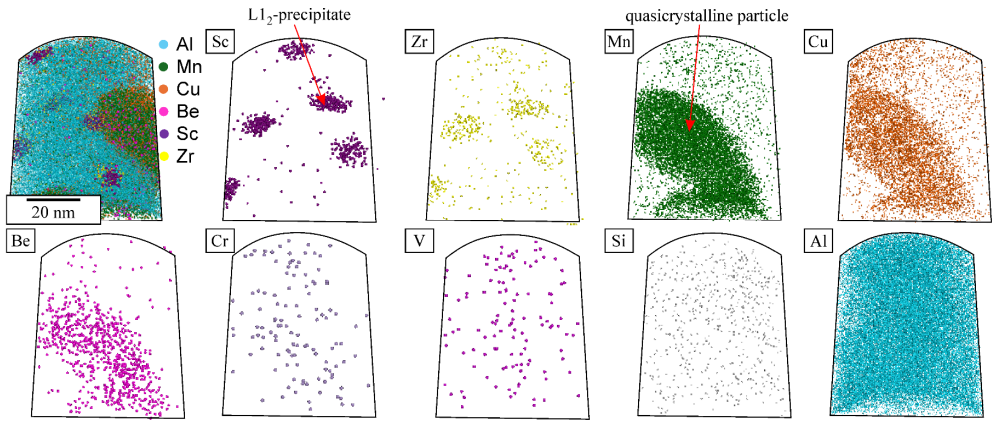

Figure 5. Elemental mapping (APT) of the heat-treated sample (the material was cast, and heat-treated at 330 °C/24 h + 450 °C/30′).

3.2. Microstructure and Properties of the Friction-Stir-Processed Zones

The hardness of the alloy in the as-cast condition was 88 ± 4 HV 0.1, while, in the heat-treated condition, it was 123 ± 5 HV 0.1. The strengthening effect in the as-cast condition arises mainly from the solid solution strengthening and partly from the hard intermetallic particles in the interdendritic region. After heat treatment, the main strengthening effect comes from the nanoscale precipitates, while the solid solution strengthening is reduced sharply.

A typical SZ shape is shown in Figure 6a. At the top, the SZ thickness was comparable to the shoulder diameter, and, at the bottom, it decreased to a value close to the pin diameter. The hardness distribution in the SZ of the as-cast specimen was rather uniform throughout the entire specimen (Figure 6b). The hardness attained was around 90 HV 0.1, which is similar to the initial hardness. The hardness line profile showed a uniform hardness within the SZ (Figure 7). Outside the SZ, at the beginning of the HAZ, the hardness dropped to a minimum hardness of about 80 HV 0.1, which indicates softening, probably by the reduction in solid solution strengthening.

The hardness in the SZ of the heat-treated sample was like that of the as-cast sample (Figure 6b,c). The minimum value was attained within the SZ and then increased slightly towards the SZ edge (Figure 7). It ranged from 110 to 120 HV 0.1 in the shallow TMAZ and exceeded 120 HV 0.1 in the HAZ. In the HAZ, the hardness jumped sharply from the value in the SZ to the hardness values after heat treatment, indicating the alloy's resistance to thermal softening. However, the decrease in the hardness in the SZ by about 25% suggests the strong mechanical softening of the heat-treated sample.

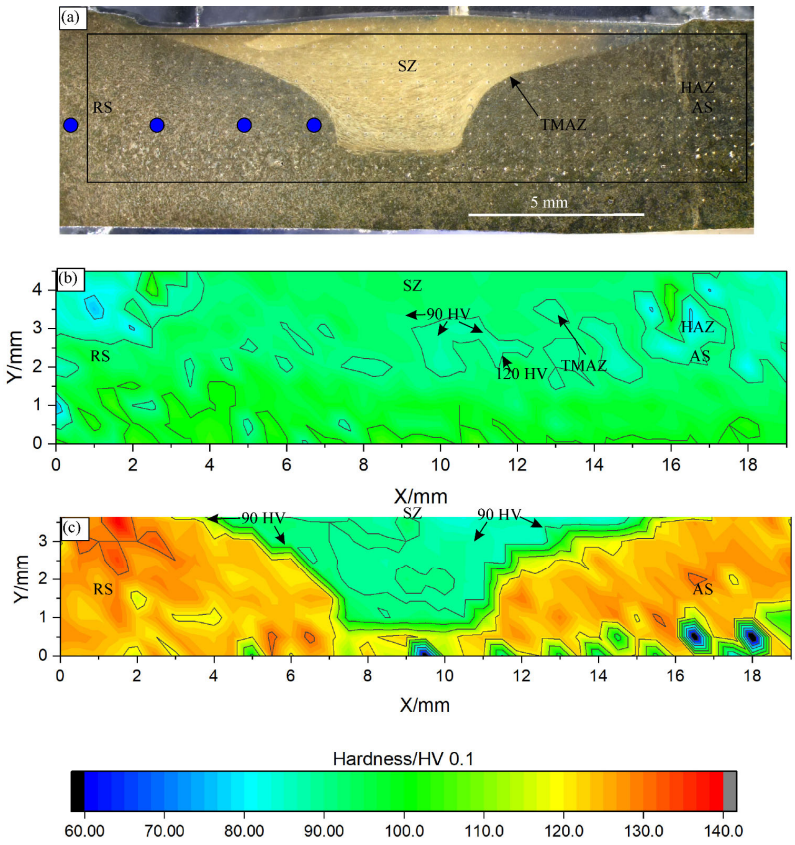

Figure 6. FSP area in the as-cast and heat-treated samples: (**a**) light micrograph of the heat-treated sample, (**b**) hardness map for the as-cast sample, and (**c**) hardness map for the heat-treated sample. The contours for 90 and 120 HV are indicated in (**b**) and (**c**). AS—advancing side, RS—retreating side, SZ—stir zone, TMAZ—thermomechanically affected zone, and HAZ—heat-affected zone. The blue circles in (**a**) indicate the temperature measuring positions.

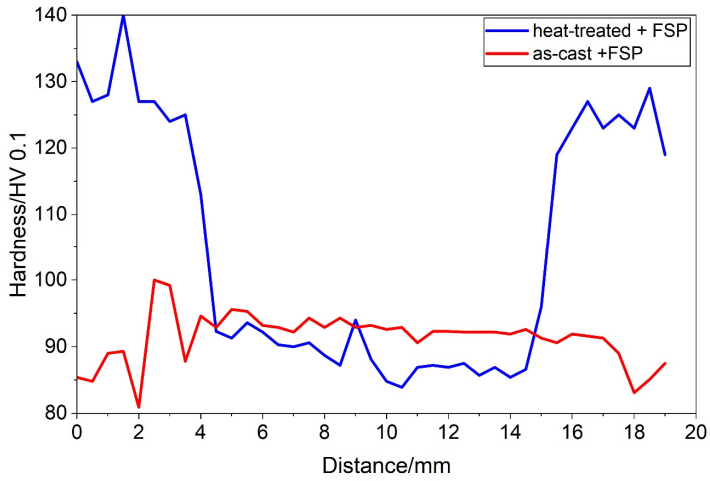

Figure 7. The hardness line profiles for the Y = 3 mm in Figure 6b,c, which is approximately 2 mm below the initial surface. The hardness line profiles for the other distances were qualitatively the same. They differed mainly in the thickness of the SZ.

During the FSP of the heat-treated sample, the temperatures were measured at several positions. The distances to the SZ edge were measured after the metallography. Figure 8 shows the temperature profiles at four positions. The maximum temperature of 533 °C was achieved close to the SZ. The temperature exceeded 500 °C for about 10 s. The maximum temperatures decreased with increasing distance from the SZ. No temperature was measured within the SZ. We may assume that the temperature was higher than 550 °C, more likely higher than 600 °C.

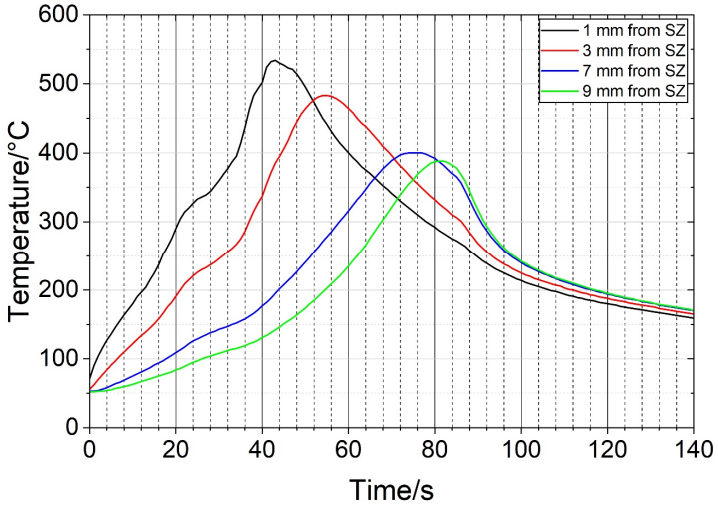

Figure 8. Temperature profiles at the positions indicated in Figure 6a (SZ—stir zone).

FSP modified the initial microstructures completely, as shown in Figure 1. The Mn-rich intermetallic phases in the interdendritic regions were crushed into dispersed particles ranging from a few tenths of nanometres up to 5 µm (Figure 9). The total fraction of particles in the SZ increased to more than 6%, regardless of the initial conditions. In contrast, the fraction of Θ-Al_2Cu decreased further, to less than 0.1%. This indicated that the temperature in the SZ reached, or even exceeded, the solvus temperature for copper. Thus, during FSP, almost all the Θ-Al_2Cu dissolved, and some particles may have reprecipitated during cooling. The dissolved Cu diffused into the Mn-rich particles, increasing their Cu content. The detailed EDS analyses in the SEM showed that the particles in the 3–5 µm range contained 17–19 at.% Mn, 2–4% Cu, 1–3 at.% Fe, and around 1 at.% Cr, while the particles

with sizes 1–3 µm contained more Cu (4–6 at.%) and less Fe and Cr. The dissolved Cu enriched the solid solution and entered partly into the Mn-rich particles, causing a transition to τ_1-$Al_{29}Mn_6Cu_4$ [17]. The SEM EDS confirmed that all the analysed Mn-rich particles with a size of less than 1 µm contained Mn and Cu, and that the atomic ratio was 3:2, corresponding to the phase τ_1-$Al_{29}Mn_6Cu_4$ (Figure 10). This phase was identified in the Al-Mn-Cu-Be alloy after FSP [17]. In the investigated alloy, its phase fraction was much lower. Nevertheless, the XRD spectra (Figure 2) revealed changes in the peak positions during FSP, indicating the presence of τ_1.

The particle distribution in SZ (Figure 11) is similar for the as-cast and heat-treated samples. The highest number of particles lies in the range below 1 µm. The crystal grains of α-Al were reduced during FSP to 0.5–3 µm, due to dynamic recovery and recrystallisation (Figure 10a).

The IQC and DQC precipitates vanished from the microstructure completely during the FSP of the heat-treated sample. The Mn- and Cu-rich particles in Figure 10 are more likely the remains of the interdendritic phases than the quasicrystalline precipitates. The EDS in STEM (Figure 12) showed clearly that most of the spherical particles with sizes 45 ± 15 nm contained Sc and Zr, and can thus be identified as $L1_2$-Al_3(Sc,Zr). Their number density was determined to be 3.0×10^{20} m^{-3}, which was about two orders of magnitude lower than after heat treatment. The τ_1 particles are mainly larger, in the range of 0.5–3 µm. They are mainly the result of the transformation of the previous Mn-rich phases into τ_1, enabled by the Cu enrichment. Since the overall fraction of intermetallic phases increased, some precipitation of τ_1 from the supersaturated solid solution was also possible. The particle in Figure 12c is a typical example.

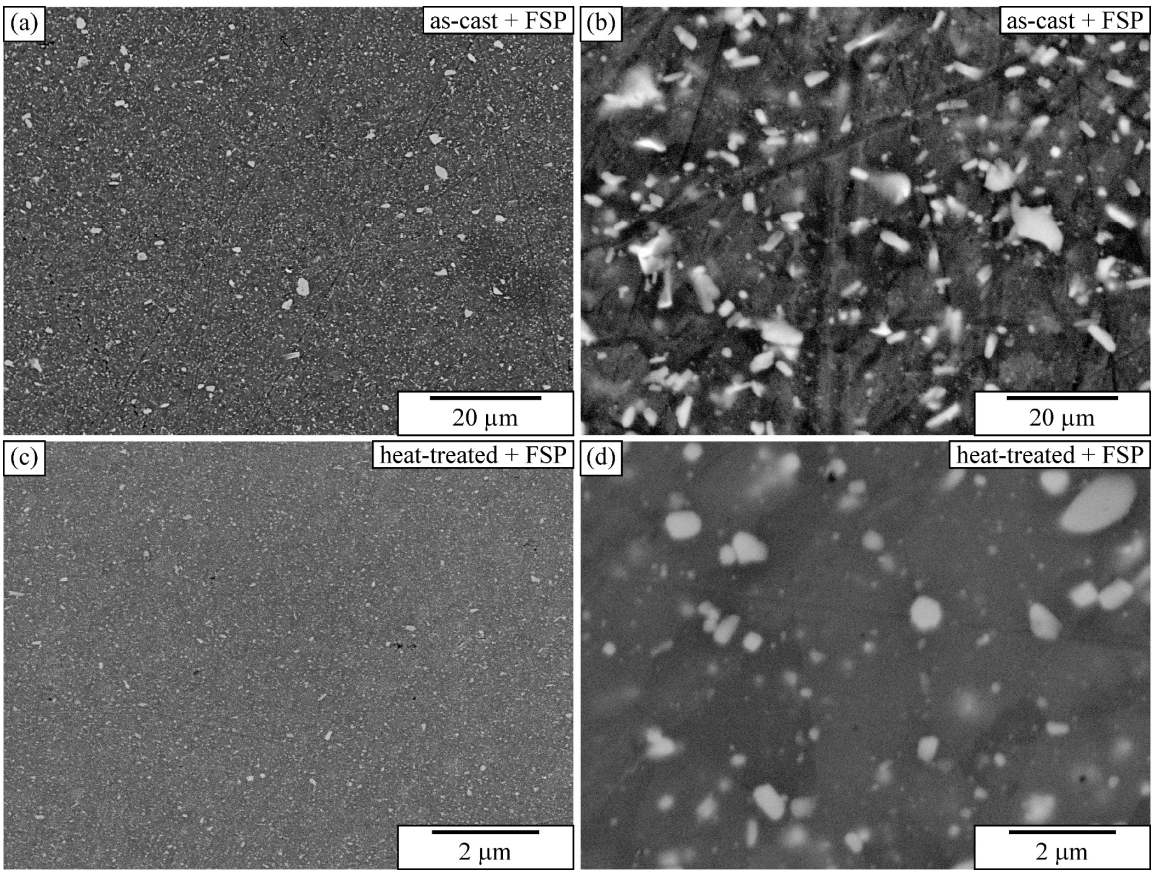

Figure 9. Backscattered electron micrograph of the SZ of (**a**,**b**) as-cast, and (**c**,**d**) heat-treated samples.

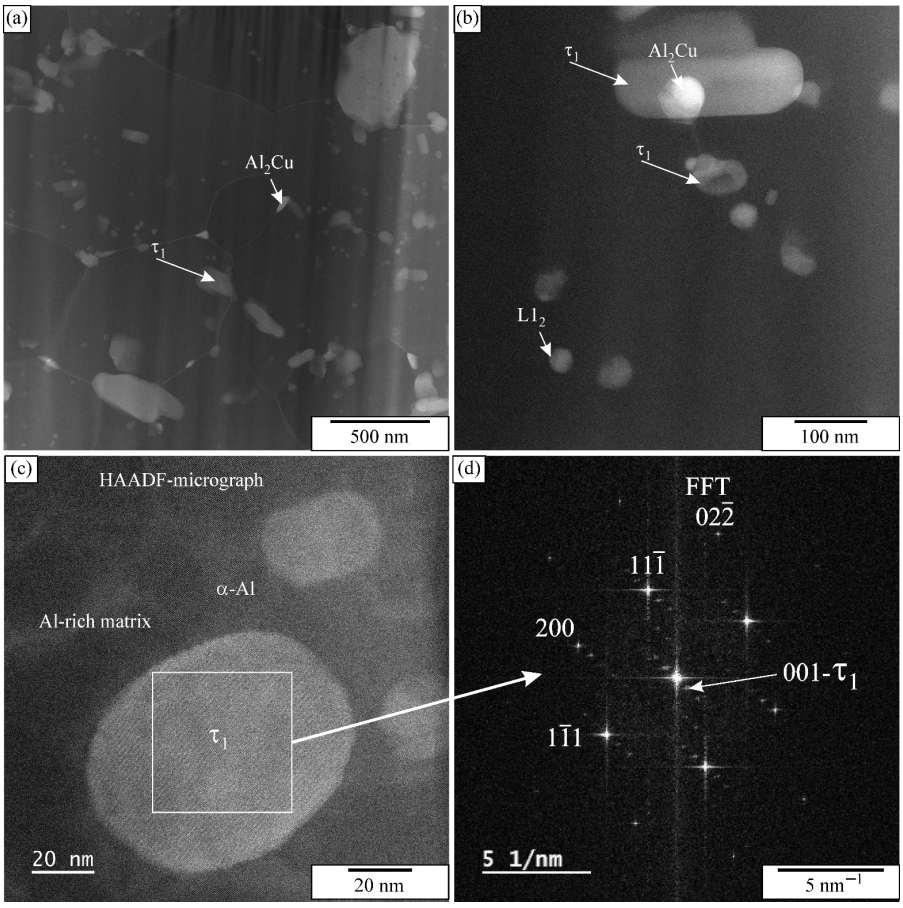

Figure 10. Phase τ_1-$Al_{29}Mn_6Cu_4$ in the investigated alloy after FSP: (**a**) HAADF micrograph showing crystal grains, (**b**) HAADF micrograph at a higher magnification, (**c**) high-resolution HAADF micrograph, and (**d**) Fast Fourier Transform (FFT) of the Al-rich matrix and τ_1-$Al_{29}Mn_6Cu_4$.

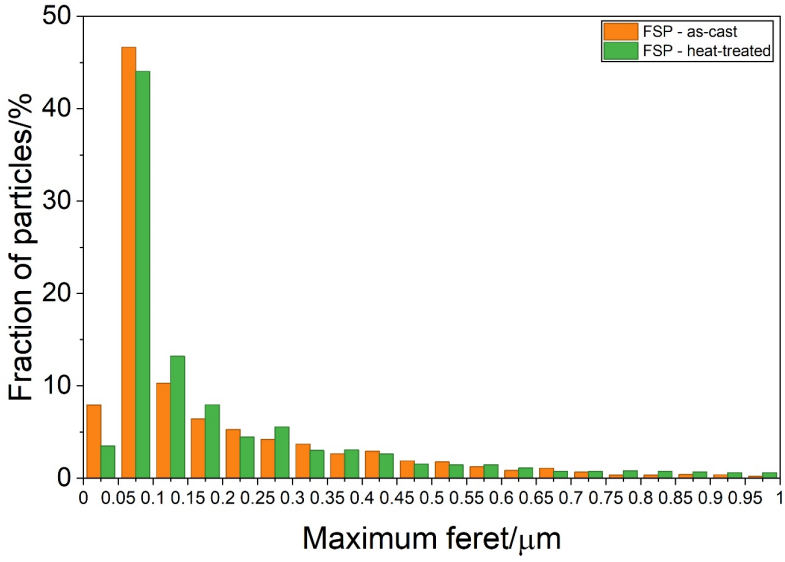

Figure 11. Particle size distribution in the stir zone of the samples initially in the as-cast (FSP—as-cast) and heat-treated (FSP—heat-treated) conditions.

The small $L1_2$-Al_3X precipitates (size 3–5 nm) were distributed uniformly in the quasicrystal PFZ and between the quasicrystalline particles in the heat-treated samples. FSP also caused the dissolution of these particles, and only some 30–50 nm-large $L1_2$-Al_3X remained in the microstructure.

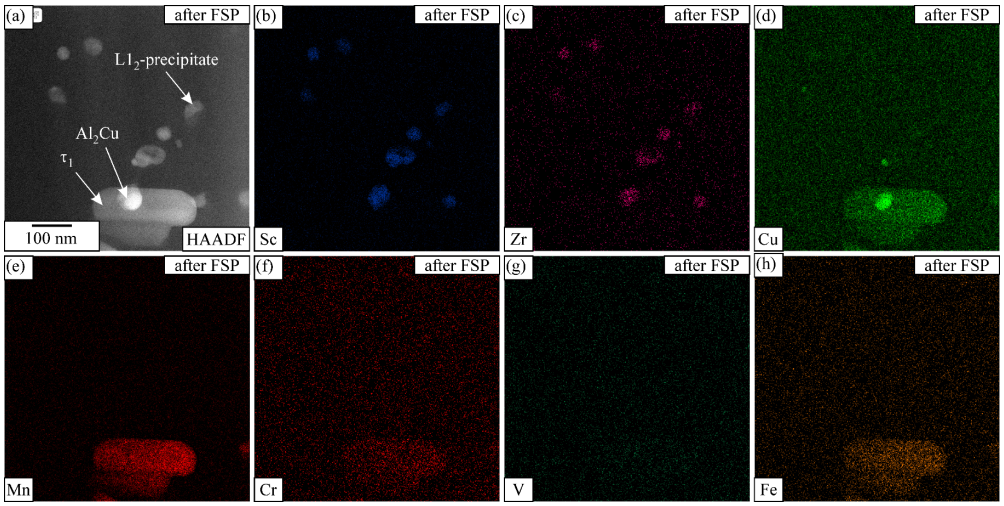

Figure 12. STEM EDS mapping in the SZ of the heat-treated sample after FSP, with each element mapping displayed by intensity. The analysed area includes the phases τ_1-$Al_{29}Mn_6Cu_4$, Θ-Al_2Cu, and $L1_2$-Al_3X. The IQC and DQC precipitates disappeared during FSP. (**a**) HAADF image, elemental maps of (**b**) Sc, (**c**) Zr, (**d**) Cu, (**e**) Mn, (**f**) Cr, (**g**) V and (**h**) Fe.

Figure 13 shows the APT distribution of the elements after FSP—namely, τ_1-$Al_{29}Mn_6Cu_4$, which also contained Be. Thus, the Be is concentrated in a phase containing Mn and Cu. No large $L1_2$ precipitates were observed in this region. Before FSP, Zr and Sc were concentrated mainly in the $L1_2$ particles, and only a few Sc and Zr atoms were in the matrix. However, after FSP, the Sc and Zr formed clusters, and the results of the TEM indicate there were no $L1_2$ precipitates with a size of 5 nm. Around the Al-Mn-Cu phase, Fe enrichment was observed. Since Fe was not observed in the initial condition, it may have arisen from steel tool dissolution.

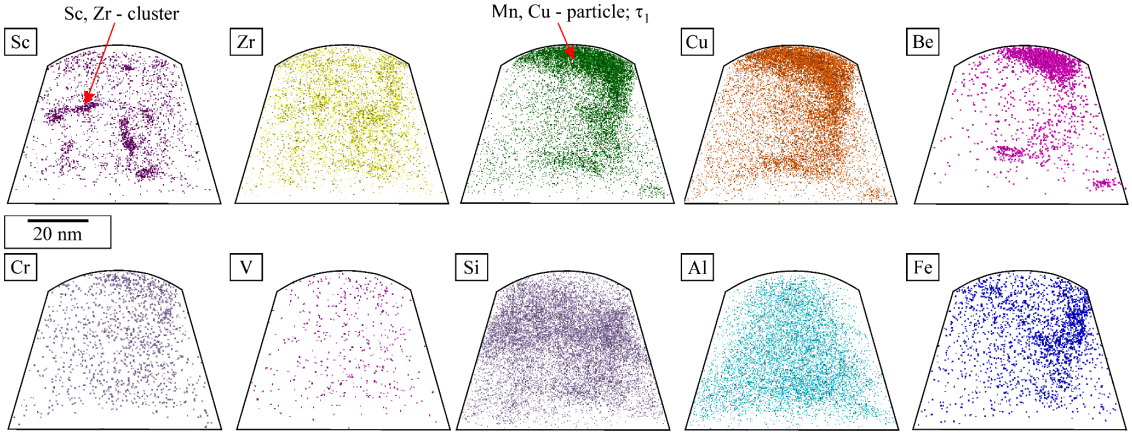

Figure 13. Elemental mapping (APT) of the alloy after FSP (rotational speed 475 min^{-1}, and lateral speed 46 mm min^{-1}).

4. Discussion

The discussion below aims to provide a plausible explanation of the processes that occur during FSP in the stir zone, based on the experimental results and the scientific literature.

At the current amounts of Mn and Cu (2.18% Mn, 2.73% Cu), α-Al, Θ-Al_2Cu, and τ_1-$Al_{29}Mn_6Cu_4$ are the stable phases in the Al-Mn-Cu phase diagram at room temperature [32]. Phase τ_1 has an orthorhombic structure. This phase often forms as rodlike precipitates in commercial Al-Mn-Cu, where it is known as the T precipitate, with a slightly different chemical composition [33]. It is also formed by the ageing of Al-Mn-Cu-Be al-

loys at temperatures above 450 °C [26,34]. Due to the increasing solubility of copper at higher temperatures, it is expected that all the amounts of Θ-Al_2Cu would dissolve above 450 °C [35]. The amounts of Be, Cr, and V in this alloy are very low; thus, no additional phases are expected. It is more likely that these elements would be incorporated in other phases. On the other hand, the amounts of Sc and Zr are sufficient to form the stable $L1_2$-Al_3(Sc,Zr) phase at all temperatures [36]. However, its fraction decreased with the increasing temperature.

The matrix is subjected to high temperatures, strain, and strain rates during FSP. Thus, it is expected that dynamic recovery and recrystallisation take place, leading to the formation of fine, micrometre-sized crystal grains [17]. The conditions in the SZ can lead to the fragmentation and dissolution of the stable and metastable phases. It is expected that all the Θ-Al_2Cu dissolves, increasing the amount of copper in the solid solution. At the same time, the metastable Mn-rich phases begin to fracture and dissolve in the matrix. When a solubility product reaches a critical value, the τ_1 phase can begin to precipitate. In addition, the dissolved copper diffuses into the fractured particles of the Mn-rich phases (Al_4Mn and IQC), starting to transform them into stable τ_1. Briefly, the fracture and dissolution of primary particles, and the precipitation of τ_1 and $L1_2$ precipitates, resulted in a fine dispersion of particles in the SZ. Such a distribution of fine particles prevented grain growth during dynamic recrystallisation.

The as-cast microstructure consisted of a supersaturated solid solution, Θ-Al_2Cu, and coarse metastable Mn-rich phases. The contribution of the solid solution strengthening by copper and manganese is estimated at 25 HV; the solid solution strengthening factors were taken from Ref. [37]. It is aligned with the hardness of 60–65 HV measured in a similar alloy after slow cooling from 600 °C [34]. Since the temperatures in the SZ are estimated to be close to 600 °C, only stable τ_1 and $L1_2$ precipitates can form during FSP, which are relatively coarse τ_1 and contribute a little to strengthening. The main strengthening effect arises from the grain boundaries. By taking a typical grain-boundary-strengthening coefficient of 0.2 [38], the grain boundary strengthening can contribute about 30 HV. Thus, the hardness after FSP remains unchanged.

The supersaturated solid solution in the as-cast state enables the formation of IQC, DQC, and $L1_2$ precipitates during ageing. The IQC particles cannot be sheared by dislocations, thereby strengthening the matrix via the Orowan mechanism [39]. Using typical values for aluminium alloys and an interparticle distance of 50 nm, the increase in strength is around 60 HV. After ageing, the reduction in solid solution strengthening is offset by dispersion strengthening, resulting in a hardness of 120–130 HV. However, during FSP, the IQC particles dissolved, while the L12 became much larger; thus, dispersion strengthening disappeared. As a result, the microstructure in the SZ becomes similar to that of the friction-stir-processed as-cast sample, with a similar hardness. A little higher hardness of the as-cast specimen can arise from a larger fraction of finer precipitates (Figure 11).

During FSP, the hardening precipitates in SZ were dissolved, resulting in a sharp decrease in hardness. Using Agren's equation for the dissolution of spherical particles [40],

$$t = \frac{r_0^2}{2\alpha D_{\mathrm{Mn}}} \tag{1}$$

where α is a dimensionless supersaturation,

$$\alpha = \frac{C_i - C_m}{C_p - C_i} \tag{2}$$

where:

Mn content in IQC: C_p = 20%;

Mn content at the interface IQC/matrix: C_i = 2%;

Mn content in matrix: C_m = 0.1%.

With this Mn content, one obtains α = 0.05.

The diffusion coefficient of Mn [41] is given as $D_0 = 1.35 \times 10^{-2}$ m^2 s^{-1}, Q = 211,500 J mol^{-1}. If we suppose a temperature of 600 °C in the SZ, the Mn diffusion coefficient is $D = 2.99 \times 10^{-15}$ m^2 s^{-1}.

By using these data, the dissolution time for 20–30 nm IQC precipitates is only 1–3 s at 600 °C (Table 1). The IQC precipitates should be larger than 100 nm to survive FSP, since the tool's dwell time is about 22 s. This is unlikely to be achieved through heat treatment. However, it could be achieved by decreasing the heat input by FSP. Table 1 shows that, at 500 °C, the dissolution time exceeds the dwell time; thus, the 20–30 nm particles will not dissolve completely. However, if we take into account pipe diffusion, then, even at 450 °C, most of the IQC precipitates will dissolve (Table 1).

Table 1. Effect of particle diameter on the dissolution time at 600 °C.

d_o/nm	t_d at 600 °C/s Static Diffusion	t_d at 550 °C/s Static Diffusion	t_d at 500 °C/s Static Diffusion	t_d at 450 °C/s Static Diffusion	t_d at 450 °C/s Enhanced Diffusion
20	1.34	7.9	58.1	565.6	11.3
30	3	17.7	130.7	1272.7	25.5
50	8	49.2	363.1	3535.2	70.7
100	33.5	196.7	1452.3	14,140.9	282.8
150	75.4	442.5	3267.8	31,816.9	636.3
200	134	786.7	5809.3	56,563.4	1131.3

The most heat is generated at the interface between the tool and the specimen [42,43]. The heat generated is proportional to the rotational speed and inversely proportional to the traverse speed. It depends on the axial force and the coefficient of friction between the tool and the specimen. Thinner tools produce less heat. With the appropriate parameters and modified tools, it could be possible to reduce the temperature in the SZ below 500 °C. This could enable the IQC precipitates to survive. If the pipe diffusion increased the diffusivity by about 50 times, as observed for Y in the Mg alloy [5], then reducing the maximum temperature to 450 °C would be necessary (Table 1).

The dissolution time for $L1_2$ precipitates is calculated to be about 10 times shorter, due to the higher diffusion coefficient of Sc relative to Mn and a smaller particle size. Thus, small $L1_2$ precipitates dissolve, and some grow. Namely, the number density of the coarse $L1_2$ after FSP is about 100 times less than the initial number density. They remain in the microstructure, since they are more thermodynamically stable than the IQC and DQC phases. The atomic cluster of Sc in the Zr atoms, as revealed by APT, probably formed during the relatively slow cooling after FSP.

Previous research revealed that Be enhances the precipitation of quasicrystalline precipitates strongly [44]. It was speculated that the Be clusters facilitate the nucleation of IQCs, and that the Be is subsequently incorporated into the IQC precipitates. This work confirms that assumption. It also stabilises the IQC phase, as it precipitates from the solid solution, even at 450 °C. There is probably also an attractive interaction with the Mn atoms, since the Be is also present in τ_1 after FSP. The exact positions of the Be atoms in the IQC and τ_1 phases are not known, and would require further investigation using APT. The positive effect of Be was also observed in the Al-Mg-Li alloys, promoting recrystallisation and reducing the precipitate-free zone [45]. In the Al-Cu-Li-Mg-Zr-Ag alloy, it affected the precipitation behaviour by accelerating the formation of GP zones and providing a more uniform distribution of the strengthening precipitates [46].

The FSP resulted in a similar distribution of particles for both initial conditions, and, consequently, in a similar hardness. There were no precipitates in the as-cast condition, and

the fine dispersion of particles was obtained by the fracturing and dissolution of the primary intermetallic phases and the precipitation of the stable τ_1 phase. On the other hand, the FSP of the heat-treated sample led to the dissolution of the IQC and DQC precipitates and the coarsening of the $L1_2$ precipitates, resulting in a sharp drop in hardness. Such a drop was also found in other Al alloys, such as Al-Mn-Si and Al-Mg-Sc [22]. The hardness was improved by post-welding ageing treatment, but this is questionable for the investigated alloy. It would be better to reduce the heat input, or apply cooling during FSP.

5. Conclusions

The main conclusions of this work are as follows:

- In the stir zone, FSP decreased the size of the dendritic Al-rich grains from about 120 μm to a few micrometres, due to dynamic recovery and recrystallisation;
- The primary Mn-rich intermetallic phases were dispersed predominantly into particles in the 0.5–3 μm range and transformed mainly into a more stable τ_1-$Al_{29}Mn_6Cu_4$ phase, which was caused by copper diffusion from the solid solution into the crushed particles;
- The fraction of dispersed particles after FSP increased due to the precipitation from the solid solution during cooling;
- The Θ-Al_2Cu dissolved mainly in the matrix during heat treatment, and the remaining part during FSP. However, it reprecipitated partly at the grain boundaries during cooling after FSP;
- The nanoscale quasicrystalline precipitates dissolved completely during FSP, while only a small number of $L1_2$ precipitates remained.
- Beryllium was present in the phases containing Mn and Cu; quasicrystalline precipitates before FSP and τ_1 after FSP;
- The FSP of the as-cast sample maintained a similar hardness, but the FSP of the heat-treated sample caused a significant mechanical softening, reducing the hardness by about 25% due to precipitate dissolution and coarsening.

The most important conclusion for future work is that quasicrystalline precipitates smaller than about 30 nm cannot survive the harsh environment during FSP. Thus, it would be necessary to optimise the heat treatment to obtain much larger quasicrystalline precipitates, e.g., at least 100 nm, or to modify the FSP parameters to adequately lower the temperature in the stir zone.

Author Contributions: Conceptualisation, F.Z., T.B. (Tonica Bončina), E.F. and D.K.; methodology, F.Z. and D.K.; validation, F.Z., T.B. (Tonica Bončina), T.B. (Torben Boll) and R.D.-B.; investigation, F.Z., P.M.P.D., Y.L., T.B. (Torben Boll), R.D.-B., L.H., E.F., D.K. and T.B. (Tonica Bončina); writing—original draft preparation, F.Z., E.F., D.K., L.H. and P.M.P.D.; writing—review and editing, F.Z., T.B. (Torben Boll), R.D.-B., T.B. (Tonica Bončina), D.K., L.H., P.M.P.D. and Y.L.; visualisation, F.Z. and Y.L.; supervision, T.B. (Torben Boll), R.D.-B. and T.B. (Tonica Bončina); project administration, T.B. (Tonica Bončina); funding acquisition, T.B. (Tonica Bončina). All authors have read and agreed to the published version of the manuscript.

Funding: This research was funded by the Slovenian Research Agency for the projects P2-0120 and I0-0029. It was funded partly by the ESTEEM (Grant Agreement 823717) and ReMade@ARI (Grant Agreement 101058414) for the STEM investigations, NFFA-Europe (Pilot no. 101007417) for the chemical analysis, and APT. The XRD investigations were carried out at Elettra, Sincrotrone Trieste, Italy, in the framework of Proposal 20245574.

Data Availability Statement: The data are currently unavailable due to the ongoing project. However, parts of the data can be obtained upon reasonable request.

Acknowledgments: We acknowledge the Ministry of Education, Science and Sport, Republic of Slovenia, and the European Union's European Regional Development Fund for the equipment

purchased within the framework "Upgrading national research infrastructures—RIUM". We thank KNMFi for the use of FIB and APT. A special thanks to Delphine Chassaing for the FIB preparation and Sabine Schlabach for the plasma-FIB preparation. While preparing this work, the authors did not use AI-assisted technologies in the writing process. The software "Grammarly (v1.2.242.1855)" was used for spelling and grammar checks. After using this tool, the authors reviewed and edited the content as needed. They take full responsibility for the publication's content.

Conflicts of Interest: Authors Yan Lu and Rafal Dunin-Borkowski were employed by the Forschungszentrum Jülich GmbH. The remaining authors declare that the research was conducted in the absence of any commercial or financial relationships that could be construed as a potential conflict of interest.

References

1. Heidarzadeh, A.; Mironov, S.; Kaibyshev, R.; Çam, G.; Simar, A.; Gerlich, A.; Khodabakhshi, F.; Mostafaei, A.; Field, D.P.; Robson, J.D.; et al. Friction stir welding/processing of metals and alloys: A comprehensive review on microstructural evolution. *Prog. Mater. Sci.* **2021**, *117*, 100752. [CrossRef]
2. Zhang, Y.; Shi, J.; Liao, G.; Li, R.; Peng, J.; Kuang, S.; Shen, F. Effects of Tool Structure and Process Parameters in Friction Stir Welding on the Temperature and Mechanical Properties of Dissimilar Copper–Aluminium Welded Joints. *Metals* **2025**, *15*, 193. [CrossRef]
3. Mishra, R.S.; Ma, Z.Y. Friction stir welding and processing. *Mater. Sci. Eng. R Rep.* **2005**, *50*, 1–78. [CrossRef]
4. Cavaliere, P.; De Marco, P.P. Friction stir processing of a Zr-modified 2014 aluminium alloy. *Mater. Sci. Eng. A* **2007**, *462*, 206–210. [CrossRef]
5. Jacquin, D.; Guillemot, G. A review of microstructural changes occurring during FSW in aluminium alloys and their modelling. *J. Mater. Process. Technol.* **2021**, *288*, 116706. [CrossRef]
6. Palanivel, S.; Arora, A.; Doherty, K.J.; Mishra, R.S. A framework for shear driven dissolution of thermally stable particles during friction stir welding and processing. *Mater. Sci. Eng. A* **2016**, *678*, 308–314. [CrossRef]
7. Kumar, A.; Kumar, V. A review of recent progress in the fabrication of surface composites through friction stir processing. *Mater. Today: Proc.* **2022**, *63*, 494–503. [CrossRef]
8. Morozova, I.; Królicka, A.; Obrosov, A.; Yang, Y.; Doynov, N.; Weiß, S.; Michailov, V. Precipitation phenomena in impulse friction stir welded 2024 aluminium alloy. *Mater. Sci. Eng. A* **2022**, *852*, 143617. [CrossRef]
9. Kang, J.; Feng, Z.-C.; Frankel, G.S.; Huang, I.W.; Wang, G.-Q.; Wu, A.-P. Friction Stir Welding of Al Alloy 2219-T8: Part I-Evolution of Precipitates and Formation of Abnormal Al2Cu Agglomerates. *Metall. Mater. Trans. A* **2016**, *47*, 4553–4565. [CrossRef]
10. Chen, J.; Chen, R.; Liao, H.; He, Y.; Chen, P.; Tian, Y.; Zhang, B.; Zhang, Z. Improving joint performance of friction stir welded 2195-O Al–Li alloy by post-weld heat treatment and rolling deformation. *J. Mater. Res. Technol.* **2024**, *29*, 5048–5059. [CrossRef]
11. Chen, C.; Liu, F.-g.; Huang, C.-p.; Xia, Y.; Xia, C.; Niu, P.-l. Comparative strengthening of intermetallic compounds produced in situ by friction stir processing on different aluminum alloy matrixes. *J. Mater. Res. Technol.* **2023**, *24*, 1816–1826. [CrossRef]
12. Vimalraj, C.; Kah, P. Experimental Review on Friction Stir Welding of Aluminium Alloys with Nanoparticles. *Metals* **2021**, *11*, 390. [CrossRef]
13. Liu, X.; Jia, R.; Cheng, W.; Zhang, H.; Tian, J.; Zhai, X. Influence of the second phase on relative fracture behavior of friction stir welded 7A52 aluminum alloy. *Mater. Today Commun.* **2022**, *33*, 104215. [CrossRef]
14. Liu, Y.; Deng, C.; Gong, B.; Bai, Y. Effects of heterogeneity and coarse secondary phases on mechanical properties of 7050-T7451 aluminum alloy friction stir welding joint. *Mater. Sci. Eng. A* **2019**, *764*, 138223. [CrossRef]
15. Vargas, M.; Lathabai, S. Microstructure and Mechanical Properties of a Friction Stir Processed Al-Zn-Mg-Cu Alloy. *Mater. Sci. Forum* **2010**, *654–656*, 1428–1431. [CrossRef]
16. Singh, V.P.; Deepak, K.; Kuriachen, B. Parametric effect on microstructure evolution, grain size and mechanical behaviour of friction stir butt welding of AA6061-T6 alloy. *J. Adhes. Sci. Technol.* **2026**, *40*, 357–381. [CrossRef]
17. Macerl, M.; Zupanič, F.; Hočuršćak, L.; Klobčar, D.; Kovács, A.; Bončina, T. Microstructure and Properties after Friction Stir Processing of Twin-Roll Cast Al-Mn-Cu-Be Alloy. *Crystals* **2022**, *12*, 630. [CrossRef]
18. Wang, Y.; Huang, Y.; Meng, X.; Wan, L.; Feng, J. Microstructural evolution and mechanical properties of MgZnYZr alloy during friction stir processing. *J. Alloys Compd.* **2017**, *696*, 875–883. [CrossRef]
19. Knipling, K.E.; Karnesky, R.A.; Lee, C.P.; Dunand, D.C.; Seidman, D.N. Precipitation evolution in Al-0.1Sc, Al-0.1Zr and Al-0.1Sc-0.1Zr (at.%) alloys during isochronal aging. *Acta Mater.* **2010**, *58*, 5184–5195. [CrossRef]
20. Shao, Q.; Elgallad, E.M.; Maltais, A.; Chen, X.G. Development of thermal-resistant Al–Zr based conductor alloys via microalloying with Sc and manipulating thermomechanical processing. *J. Mater. Res. Technol.* **2023**, *25*, 7528–7545. [CrossRef]

21. Zupanič, F.; Žist, S.; Albu, M.; Letofsky-Papst, I.; Burja, J.; Vončina, M.; Bončina, T. Dispersoids in Al-Mg-Si Alloy AA 6086 Modified by Sc and Y. *Materials* **2023**, *16*, 2949. [CrossRef] [PubMed]
22. Sauvage, X.; Dédé, A.; Muñoz, A.C.; Huneau, B. Precipitate stability and recrystallisation in the weld nuggets of friction stir welded Al–Mg–Si and Al–Mg–Sc alloys. *Mater. Sci. Eng. A* **2008**, *491*, 364–371. [CrossRef]
23. Sun, Y.B.; Chen, X.P.; Xie, J.; Wang, C.; An, Y.F.; Liu, Q. High strain rate superplasticity and secondary strain hardening of Al-Mg-Sc-Zr alloy produced by friction stir processing. *Mater. Today Commun.* **2022**, *33*, 104217. [CrossRef]
24. Mochugovskiy, A.G.; Chukwuma, E.U.; Tabachkova, N.Y.; Mikhaylovskaya, A.V. The chemical composition influence on the microstructure and superplasticity of the Al-Mg-Si-Zr-Sc-based alloys. *Mater. Sci. Eng. A* **2025**, *928*, 148063. [CrossRef]
25. Zupanič, F.; Gspan, C.; Burja, J.; Bončina, T. Quasicrystalline and L12 precipitates in a microalloyed Al-Mn-Cu alloy. *Mater. Today Commun.* **2020**, *22*, 100809. [CrossRef]
26. Zupanič, F.; Wang, D.; Gspan, C.; Bončina, T. Precipitates in a quasicrystal-strengthened Al–Mn–Be–Cu alloy. *Mater. Charact.* **2015**, *106*, 93–99. [CrossRef]
27. Bončina, T.; Zupanič, F. Metallography of Quasicrystals in Al-Alloys. *Materials* **2025**, *18*, 4575. [CrossRef]
28. Singh, A.; Ranganathan, S. On the indexing and reciprocal space of icosahedral quasicrystal. *J. Mater. Res.* **1999**, *14*, 4182–4187. [CrossRef]
29. Fung, K.K.; Zhou, Y.Q. Direct observation of the transformation of the icosahedral phase in (Al6Mn)1−xSix, into α(AlMnSi). *Philos. Mag. B* **1986**, *54*, L27–L31. [CrossRef]
30. Li, J.-F.; Ye, Z.-H.; Liu, D.-Y.; Chen, Y.-L.; Zhang, X.-H.; Xu, X.-Z.; Zheng, Z.-Q. Influence of Pre-deformation on Aging Precipitation Behavior of Three Al–Cu–Li Alloys. *Acta Metall. Sin. (Engl. Lett.)* **2017**, *30*, 133–145. [CrossRef]
31. Knipling, K.E.; Seidman, D.N.; Dunand, D.C. Ambient- and high-temperature mechanical properties of isochronally aged Al-0.06Sc, Al-0.06Zr and Al-0.06Sc-0.06Zr (at.%) alloys. *Acta Mater.* **2011**, *59*, 943–954. [CrossRef]
32. Lukas, H.L. Al-Cu-Mn (Aluminium-Copper-Manganese). In *Landolt-Börnstein-Group IV Physical Chemistry, Numerical Data and Functional Relationships in Science and Technology*; Effenberg, G., Ilyenko, S., Eds.; Springer Materials—The Landolt-Börnstein Database; Springer: Berlin/Heidelberg, Germany, 1991; Volume 11, Available online: https://materials.springer.com/lb/docs/sm_lbs_978-3-540-31687-9_5 (accessed on 1 March 2026).
33. Shen, Z.; Liu, C.; Ding, Q.; Wang, S.; Wei, X.; Chen, L.; Li, J.; Zhang, Z. The structure determination of Al20Cu2Mn3 by near atomic resolution chemical mapping. *J. Alloys Compd.* **2014**, *601*, 25–30. [CrossRef]
34. Zupanič, F.; Bončina, T. Heat-Resistant Al-Alloys with Quasicrystalline and L12-Precipitates. *Solid State Phenom.* **2022**, *327*, 26–32. [CrossRef]
35. Predel, B. Al-Cu (Aluminum-Copper): Datasheet from Landolt-Börnstein—Group IV Physical Chemistry · Volume 5A: "Ac-Au–Au-Zr". In *Springer Materials*; Springer: Berlin/Heidelberg, Germany, 2004. [CrossRef]
36. Raghavan, V. Al-Cr-Sc-Zr (Aluminum-Chromium-Scandium-Zirconium). *J. Phase Equilibria Diffus.* **2012**, *33*, 71–72. [CrossRef]
37. Ryen, Ø.; Holmedal, B.; Nijs, O.; Nes, E.; Sjölander, E.; Ekström, H.-E. Strengthening mechanisms in solid solution aluminum alloys. *Metall. Mater. Trans. A* **2006**, *37*, 1999–2006. [CrossRef]
38. Lin, C.-Y.; Lui, T.-S.; Chen, L.-H.; Hung, F.-Y. Hall-Petch Tensile Yield Stress and Grain Size Relation of Al5Mg0.5Mn Alloy in Friction-Stir-Processed and Post-Thermal-Exposed Conditions. *Mater. Trans.* **2014**, *55*, 357–362. [CrossRef]
39. Ma, K.; Wen, H.; Hu, T.; Topping, T.D.; Isheim, D.; Seidman, D.N.; Lavernia, E.J.; Schoenung, J.M. Mechanical behavior and strengthening mechanisms in ultrafine grain precipitation-strengthened aluminum alloy. *Acta Mater.* **2014**, *62*, 141–155. [CrossRef]
40. Agren, J. Kinetics of Carbide Dissolution. *Scand. J. Metall.* **1990**, *19*, 2–8.
41. Du, Y.; Chang, Y.A.; Huang, B.Y.; Gong, W.P.; Jin, Z.P.; Xu, H.H.; Yuan, Z.H.; Liu, Y.; He, Y.H.; Xie, F.Y. Diffusion coefficients of some solutes in fcc and liquid Al: Critical evaluation and correlation. *Mater. Sci. Eng. A-Struct. Mater. Prop. Microstruct. Process.* **2003**, *363*, 140–151. [CrossRef]
42. El-Sayed Seleman, M.M.; Ataya, S.; Alrasheedi, N.H.; Ahmed, M.M.Z.; Reyad, H.A.; Bakkar, A.; Fouad, R.A. Optimization of Critical Parameters in Friction Stir Spot Welding of AA5052 Aluminum Alloy Using Response Surface Methodology. *Crystals* **2025**, *15*, 571. [CrossRef]
43. Hossfeld, M. On Friction, Heat Input, and Material Flow Initiation during Friction Stir Welding: Tool and Process Optimization. *J. Manuf. Mater. Process.* **2023**, *7*, 34. [CrossRef]
44. Bončina, T.; Albu, M.; Zupanič, F. Ageing of Al-Mn-Cu-Be Alloys for Stimulating Precipitation of Icosahedral Quasicrystals. *Metals* **2020**, *10*, 937. [CrossRef]

45. Huang, Y.; Li, W.; Wu, M.; Xiao, D.; Huang, L.; Liu, W. Effects of Beryllium Addition on Microstructure, Mechanical and Corrosion Performance of Al-Mg-Li Alloys. *Materials* **2023**, *16*, 6308. [CrossRef]
46. Kim, J.K.; Chung, D.-S.; Park, H.S.; Enoki, M. Effect of Be Addition on the Precipitation Behaviors and Mechanical Properties in Al-Cu-Li-Mg-Zr-(Ag) Alloys. *Mater. Sci. Forum* **2005**, *475–479*, 381–384. [CrossRef]